Focusing Multistatic GEO SAR With Two Stationary Receivers Based on Spectrum Gap Alignment and Recovery

Yukun Guo, Ze Yu, *Member, IEEE*, Jingwen Li, and Chunsheng Li

***Abstract*—Multistatic synthetic aperture radar (SAR) composed of a geosynchronous SAR illuminator and two stationary receivers has the ability to continuously monitor areas of interest. The spatially variant azimuth wavenumber spectrum gap caused by the limited synthetic aperture time may result in a high sidelobe level, which leads to artifacts in the image. This article exploits the spatial invariance of the gap length and proposes a new imaging method to fill the spectrum gap via gap alignment and data recovery. The spectrum gaps of all the targets are aligned based on spectrum shifting, and the full spectrum is recovered using spectrum estimation. Simulation results of point targets and extended targets verify the superiority of the proposed method compared to existing algorithms.**

***Index Terms*—Geosynchronous synthetic aperture radar (GEO SAR), multistatic SAR, SAR imaging.**

I. Introduction

GEOSYNCHRONOUS synthetic aperture radar (GEO SAR) is a spaceborne imaging radar that operates at a height of approximately 36 000 km [1], [2], [3], [4], [5], [6], [7], [8], [9], [10], [11], [12], [13], [14]. By receiving the backscatter signal of the GEO SAR illuminator, a multistatic configuration can be formed with two stationary receivers, located on high towers in mountain areas or the seashore [15], [16], [17], [18], observing the same area. This multistatic system not only has the daily revisit feature of GEO SAR but also benefits from the flexibility of the receiver positions which enables multiangle information obtaining and resolution enhancement, which can be applied to regional disaster monitoring. While synchronization is an important part of implementing the multistatic system, it is assumed in this article that the synchronization issue has been resolved, and this article mainly deals with the imaging algorithm.

This article considers a multistatic GEO SAR system with two stationary receivers distributed along the azimuth direction. To achieve short-time imaging, the data acquisition time is reduced, which results in data gaps in the targets' spectrum support region, resulting in a high azimuth sidelobe level, which may lead to artifacts in imaging results. An imaging method proposed by Nithirochananont et al. [21] coherently combines the images of the bistatic pairs in the multistatic system, whereas the high sidelobe level caused by limited aperture time is not considered. Larsson et al. [22] introduced data gap filling into SAR imaging to acquire fine images. The method uses adaptive filters to estimate the missing data in the phase history, which works well when the spectrum data and spectrum gaps are aligned. Since the support region of the wavenumber spectrum in multistatic GEO SAR varies with target positions, the gap location is also spatially variant, which indicates that the spectrum gap-filling method cannot be implemented directly. Guo et al. [16] unified the spectrum support region of each receiver using spectrum shifting and range-Doppler mapping and extrapolated the spectrum using an autoregressive model. Although the method can lower the azimuth sidelobe level, the effect is not satisfactory in noisy conditions.

This article proposes a new imaging method for multistatic GEO SAR with two stationary receivers. The key of the method is to align the spectrum gaps in the wavenumber domain for all the targets using a phase function. After spectrum alignment, the gap positions as well as the spectrum support regions of all the targets in each range are identical, and the data in the spectrum gap can then be estimated and recovered to obtain the full spectrum, leading to better imaging quality.

The rest of this article is structured as follows. Section II introduces the geometry of multistatic GEO SAR with two stationary receivers and analyzes the spectrum model. Section III describes the method for spectrum gap alignment. In Section IV, a new imaging algorithm for multistatic GEO SAR with two stationary receivers is proposed. Simulation results are presented in Section V, and the computational load and the influence of target elevation are discussed in Section VI. Section VII concludes this article.

II. Imaging Geometry and Signal Model

The imaging geometry of multistatic GEO SAR with two stationary receivers is shown in Fig. 1. The scene center is set to be the origin of the Cartesian coordinates *OXYZ*, where the direction of the *y*-axis is the GEO SAR velocity vector projection onto the ground plane at the aperture center time. The *z*-axis is parallel to the normal vector of the ground plane, and the *x*-axis completes the right-handed coordinate system. The two

Manuscript received 13 September 2023; revised 6 November 2023; accepted 8 December 2023. Date of publication 13 December 2023; date of current version 28 December 2023. *(Corresponding author: Ze Yu.)*

The authors are with the School of Electronics and Information Engineering, Beihang University, Beijing 100191, China (e-mail: venik123@buaa.edu.cn; yz613@buaa.edu.cn; lijingwen@buaa.edu.cn; 00178@buaa.edu.cn).

Digital Object Identifier 10.1109/JSTARS.2023.3342486

© 2023 The Authors. This work is licensed under a Creative Commons Attribution-NonCommercial-NoDerivatives 4.0 License. For more information, see https://creativecommons.org/licenses/by-nc-nd/4.0/

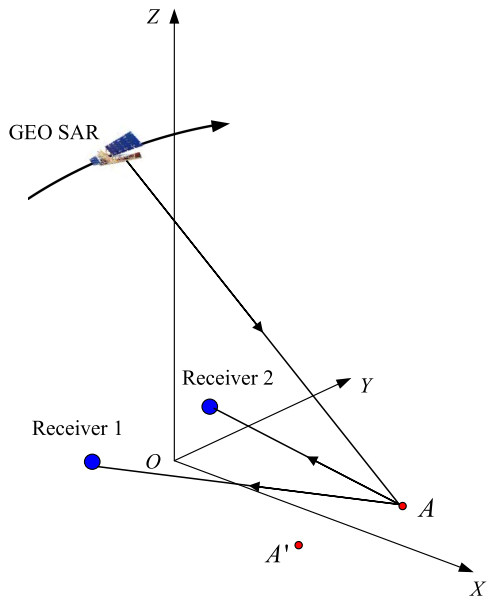

Fig. 1. Imaging geometry of multistatic GEO SAR with two stationary receivers.

stationary receivers are placed along the *y*-axis and their antenna beams cover the same area. Point $A(x_0, y_0, 0)$ is an arbitrary point in the ground plane and *B* is a point in the vicinity of *A*. Denote the coordinates of the GEO SAR transmitter and the two receivers as $(x_{\mathrm{tr}}, y_{\mathrm{tr}}, z_{\mathrm{tr}})$, $(x_{\mathrm{re},1}, y_{\mathrm{re},1}, z_{\mathrm{re},1})$, and $(x_{\mathrm{re},2}, y_{\mathrm{re},2}, z_{\mathrm{re},2})$.

To analyze the influence of synthetic aperture time on imaging, the ambiguity function model of the multistatic system is introduced first.

A. Ambiguity Function Model

Assuming that the range signal spectrum and the antenna pattern are modeled by rectangular shape functions, the ambiguity function of the bistatic configuration consisting of GEO SAR and the *k*th receiver can be derived as [23]

$$\chi_k(\mathbf{r}_A, \mathbf{r}_B) = \exp\left\{j\frac{2\pi\delta_R}{\lambda}\right\}\mathrm{sinc}\left(\frac{B_r\delta_R}{c}\right)\mathrm{sinc}\left(T_s\delta_f\right) \quad k=1,2 \tag{1}$$

where $\mathbf{r}_A$ and $\mathbf{r}_B$ are the position vector of *A* and *B*, respectively, δ_R and δ_f are the bistatic range difference and the Doppler frequency difference between *B* and *A*, respectively, λ is the wavelength of GEO SAR, B_r is the bandwidth of the range signal, c is the speed of light, and T_s is the synthetic aperture time.

When point *B* is in the ground range plane, δ_R and δ_f can be expressed as

$$\delta_R \approx \mathbf{u}_{g,k}^{\mathrm{T}}(\mathbf{r}_B - \mathbf{r}_A) \tag{2}$$

$$\delta_f \approx \boldsymbol{\Gamma}_g^{\mathrm{T}}(\mathbf{r}_B - \mathbf{r}_A) \tag{3}$$

where $\mathbf{u}_{g,k}$ ($k=1,2$) is the ground projection of the bistatic range gradient vector, $(\cdot)^{\mathrm{T}}$ denotes the transpose operator, and $\boldsymbol{\Gamma}_g$ is the ground projection of the Doppler centroid gradient vector.

Considering (1)–(3), the ground plane ambiguity function of the bistatic configuration consisting of GEO SAR and the *k*th receiver is modeled as

$$\begin{aligned}&\chi_k(\mathbf{r}_A, \mathbf{r}_B)\\ &= \exp\left\{j\frac{2\pi}{\lambda}\mathbf{u}_{g,k}^{\mathrm{T}}(\mathbf{r}_B - \mathbf{r}_A)\right\}\mathrm{sinc}\left[\frac{B_r}{c}\mathbf{u}_{g,k}^{\mathrm{T}}(\mathbf{r}_B - \mathbf{r}_A)\right]\\ &\quad\times\mathrm{sinc}\left[T_s\boldsymbol{\Gamma}_g^{\mathrm{T}}(\mathbf{r}_B - \mathbf{r}_A)\right], k=1,2.\end{aligned} \tag{4}$$

Based on (4), the ambiguity function of multistatic GEO SAR with two stationary receivers can be expressed as

$$\begin{aligned}&\chi(\mathbf{r}_A, \mathbf{r}_B)\\ &= \frac{1}{2}\sum_{k=1}^{2}\chi_k(\mathbf{r}_A, \mathbf{r}_B)\\ &= \frac{1}{2}\mathrm{sinc}\left[T_s\boldsymbol{\Gamma}_g^{T}(\mathbf{r}_B - \mathbf{r}_A)\right]\\ &\quad\times\sum_{k=1}^{2}\exp\left\{j\frac{2\pi}{\lambda}\mathbf{u}_{g,k}^{T}(\mathbf{r}_B - \mathbf{r}_A)\right\}\mathrm{sinc}\left[\frac{B_r}{c}\mathbf{u}_{g,k}^{T}(\mathbf{r}_B - \mathbf{r}_A)\right].\end{aligned} \tag{5}$$

It is indicated in (5) that the antenna patterns of the two receivers are rectangular with the same amplitude. Although the antenna patterns of the receivers may not be uniform, they can be estimated from the echo of each receiver separately and the antenna weighting can be removed. Thus the model in (5) is still applicable. Suppose an equivalent bistatic system contains the GEO SAR transmitter and a virtual receiver placed at the midpoint of the line between the two receivers, which is denoted as point *M*. The tangential direction of the iso-bistatic-range curve of the equivalent bistatic system in the ground plane can be defined as the azimuth direction of the multistatic system.

The azimuth ambiguity function can be expressed as

$$\begin{aligned}&\chi(\mathbf{r}_B - \mathbf{r}_A)\\ &= \exp\left\{j\frac{2\pi}{\lambda}\mathbf{u}_{g,M}^{T}(\mathbf{r}_B - \mathbf{r}_A)\right\}\mathrm{sinc}\left[T_s\boldsymbol{\Gamma}_g^{T}(\mathbf{r}_B - \mathbf{r}_A)\right]\\ &\quad\times\cos\left[\frac{\pi}{\lambda R_{re,M}}\mathbf{d}^{T}(\mathbf{r}_B - \mathbf{r}_A)\right]\end{aligned} \tag{6}$$

where $\mathbf{u}_{g,M}$ is the ground projection of the bistatic range gradient vector of the equivalent system, $R_{re,M}$ is the receiving range from the target to *M*, and $\mathbf{d}$ is the vector pointing from one receiver to the other.

It is shown in (6) that the azimuth ambiguity function contains three parts. The first term is a constant phase. The second term is the azimuth ambiguity function of the equivalent bistatic system, and the last term is the receiving array factor. It is indicated in (6) that once the distribution of the receivers is fixed, the array factor and the equivalent bistatic system are determined, and the sidelobe level is related to the synthetic aperture time. Fig. 2 illustrates the azimuth profiles with different synthetic aperture times. The system parameters are listed in Table I. When the synthetic aperture time is 1057 s, the multistatic ambiguity function can be considered as a bistatic ambiguity function weighted by

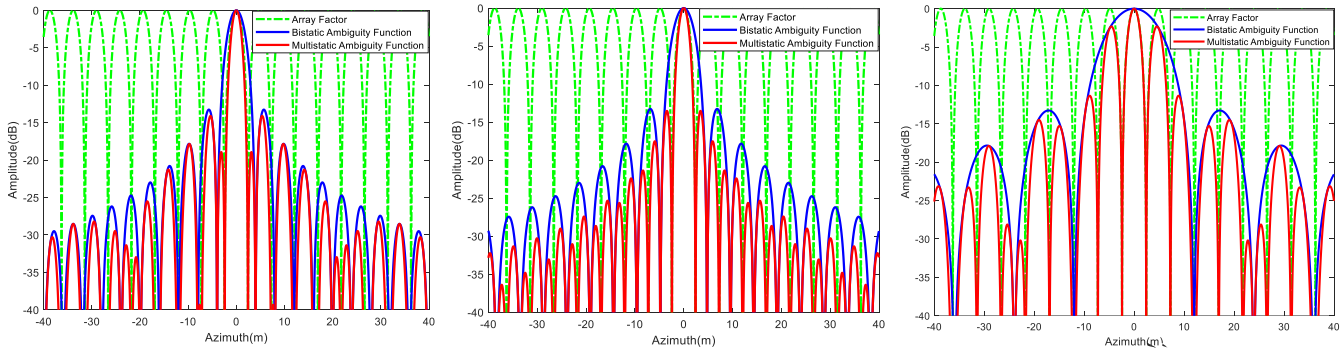

Fig. 2. Azimuth profiles with different synthetic aperture time. (a) $T_s = 1057$ s. (b) $T_s = 881$ s. (c) $T_s = 352$ s.

TABLE I
SYSTEM PARAMETERS

Parameter	Value
Semimajor axis (km)	42 164
Inclination (°)	60
Eccentricity	0
Receiver 1 Coordinate (m)	(-8000,-200,1000)
Receiver 2 Coordinate (m)	(-8000,200,1000)
Wavelength (m)	0.24
Bandwidth (MHz)	60

the array factor, resulting in a low sidelobe level. When the zero points of the array factor coincide with the peaks of the bistatic sidelobe, the highest sidelobe level of the multistatic ambiguity function is around -13 dB. As the synthetic aperture time further decreases, the sidelobe of the multistatic ambiguity function can be seen as the array function weighted by the mainlobe of the bistatic ambiguity function, and the level is higher than -13 dB, resulting in artifacts in imaging results.

B. Wavenumber Spectrum Analysis

This section analyzes the relationship between the sidelobe level and the wavenumber spectrum.

The wavenumber spectrum of point *A* can be modeled as [24]

$$S(K_x, K_y) = \exp(-jK_x x_0 - jK_y y_0) \tag{7}$$

where K_x and K_y are the wavenumber of *X* and *Y* directions, respectively.

The wavenumber spectrum of the multistatic GEO SAR system is the sum of the spectrum of the two bistatic pairs. The spectrum support region of each bistatic pair is restricted by [16]

$$\begin{cases} K_x = \frac{2\pi(f_c+f_r)}{c}\left[\frac{x_0-x_{\text{tr}}(t)}{R_{\text{tr}}(t;x_0,y_0)} + \frac{x_0-x_{\text{re},k}}{R_{\text{re},k}(x_0,y_0)}\right] \\ K_y = \frac{2\pi(f_c+f_r)}{c}\left[\frac{y_0-y_{\text{tr}}(t)}{R_{\text{tr}}(t;x_0,y_0)} + \frac{y_0-y_{\text{re},k}}{R_{\text{re},k}(x_0,y_0)}\right] \\ -B_r/2 \le f_r \le B_r/2 \\ -T_s/2 \le t \le T_s/2 \end{cases} \tag{8}$$

where $f_c = c/\lambda$ is the carrier frequency, f_r is the range frequency, and $R_{\text{tr}}(t; x_0, y_0)$ is the transmitting range history of *A* given by

$$R_{\text{tr}}(t; x_0, y_0) = \sqrt{[x_0 - x_{\text{tr}}(t)]^2 + [y_0 - y_{\text{tr}}(t)]^2 + z_{\text{tr}}^2(t)} \tag{9}$$

and $R_{\text{re},k}(x_0, y_0)$ is the range between *A* and the *k*th receiver given as

$$R_{\text{re},k}(x_0, y_0) = \sqrt{(x_0 - x_{\text{re},k})^2 + (y_0 - y_{\text{re},k})^2 + z_{\text{re},k}^2}. \tag{10}$$

The spectrum gap length can be defined as

$$L_{\text{gap}} = \sqrt{(K_{xc,1} - K_{xc,2})^2 + (K_{yc,1} - K_{yc,2})^2} - \frac{B_1 + B_2}{2} \tag{11}$$

where $K_{xc,k}$ and $K_{yc,k}$ are the wavenumber spectrum center

$$\begin{cases} K_{xc,k} = \frac{2\pi}{\lambda}\left[\frac{x_0-x_{\text{tr}}(0)}{R_{\text{tr}}(0;x_0,y_0)} + \frac{x_0-x_{\text{re},k}}{R_{\text{re},k}(x_0,y_0)}\right] \\ K_{yc,k} = \frac{2\pi}{\lambda}\left[\frac{y_0-y_{\text{tr}}(0)}{R_{\text{tr}}(0;x_0,y_0)} + \frac{y_0-y_{\text{re},k}}{R_{\text{re},k}(x_0,y_0)}\right] \end{cases}. \tag{12}$$

B_1 and B_2 are the azimuth wavenumber bandwidth of the two bistatic pairs. The negative gap length represents the overlapping length of the spectrum.

Fig. 3 illustrates the spectrum support region with different synthetic aperture times. It is shown that the ratio of azimuth spectrum gap length to bandwidth increases as the aperture time decreases. Thus it can be inferred from Figs. 2 and 3 that the sidelobe level lowers as the spectrum gap length decreases. Ignoring the antenna weighting, the sidelobe level is higher than -13 dB when the spectrum gap exists (see Appendix for details). To suppress artifacts caused by the high sidelobe, spectrum gap filling can be implemented [22]. However, it is indicated in (8) that the spectrum support region is related to the target coordinate, which means the gap is spatially variant [16], causing difficulty in filling the spectrum gap of all the targets at the same time.

III. SPECTRUM GAP ALIGNMENT

To solve the problem mentioned earlier, this article introduces an imaging method that aligns and fills the spectrum gap of all the targets in the scene.

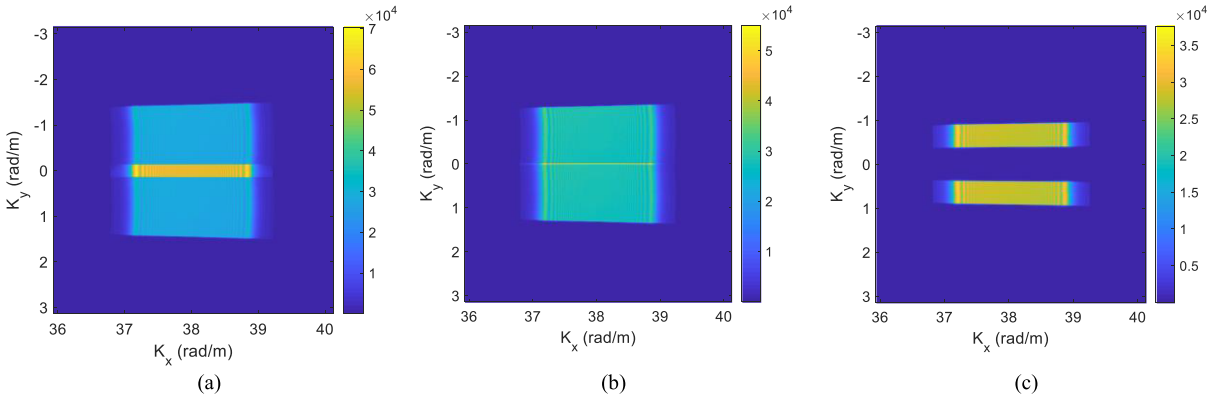

Fig. 3. Illustration of spectrum support region with different synthetic aperture time. (a) $T_s = 1057$ s. (b) $T_s = 881$ s. (c) $T_s = 352$ s.

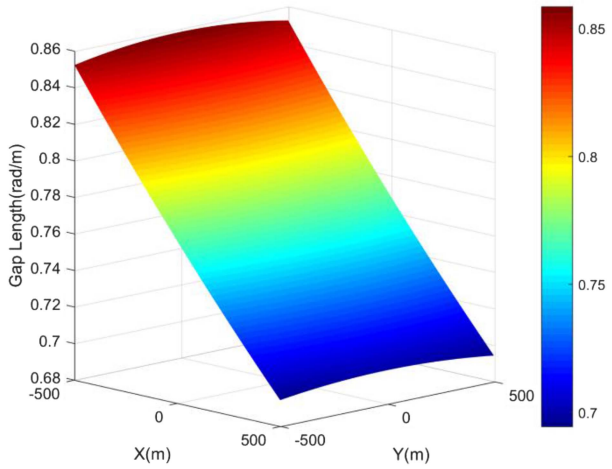

Fig. 4. Spectrum gap length.

The spectrum gap length in (11) can be approximately expressed as

$$L_{\text{gap}} \approx \frac{2\pi}{\lambda}\left(b_0 + b_{1,x}x\right) - \frac{B_1 + B_2}{2} \tag{13}$$

where

$$\begin{cases} b_0 = \sqrt{\frac{x_{\text{re},1}^2+y_{\text{re},1}^2}{R_{10}^2} + \frac{x_{\text{re},2}^2+y_{\text{re},2}^2}{R_{20}^2} - \frac{2(x_{\text{re},1}x_{\text{re},2}+y_{\text{re},1}y_{\text{re},2})}{R_{10}R_{20}}} \\ b_{1,x} = \frac{1}{b_0}\left[\frac{x_{\text{re},1}+x_{\text{re},2}}{R_{10}R_{20}} - \frac{(x_{\text{re},1}x_{\text{re},2}+y_{\text{re},1}y_{\text{re},2})}{R_{10}R_{20}}\left(\frac{x_{\text{re},1}}{R_{10}^2} + \frac{x_{\text{re},2}}{R_{20}^2}\right)\right. \\ \left. - \frac{x_{\text{re},1}z_{\text{re},1}^2}{R_{10}^4} - \frac{x_{\text{re},2}z_{\text{re},2}^2}{R_{20}^4}\right] \\ R_{10} = \sqrt{x_{\text{re},1}^2 + y_{\text{re},1}^2 + z_{\text{re},1}^2} \\ R_{20} = \sqrt{x_{\text{re},2}^2 + y_{\text{re},2}^2 + z_{\text{re},2}^2} \\ B_1 = 0.886\frac{2\pi}{\rho_{1,a}} \\ B_2 = 0.886\frac{2\pi}{\rho_{2,a}} \end{cases} \tag{14}$$

where $\rho_{1,a}$ and $\rho_{2,a}$ are the azimuth resolutions of the bistatic pairs. Since the azimuth resolutions are almost the same in the scene [25], the bandwidth B_1 and B_2 are considered as constants. Fig. 4 illustrates the azimuth wavenumber spectrum gap length in an area of 1 km × 1 km. Therefore, it is indicated that gap length only relates to the range coordinate, which means that the spectrum gaps of the same range coordinate can be filled after shifting the spectrum center to the same position.

Define the wavenumber spectrum center (K_{xc}, K_{yc}) of the multistatic system as

$$\begin{cases} K_{xc} = \frac{1}{2}\left(K_{xc,1} + K_{xc,2}\right) \\ K_{yc} = \frac{1}{2}\left(K_{yc,1} + K_{yc,2}\right) \end{cases}. \tag{15}$$

Denote the ground plane imaging results as $I(x, y)$. To align the spectrum gap of all targets, a phase function in the spatial domain

$$g\left(x, y\right) = \exp\left\{j\phi\left(x, y\right)\right\} \tag{16}$$

is designed as follows. The spectrum shifting is implemented by multiplying the phase function $g(x, y)$ with the imaging result $I(x, y)$, namely

$$I_{\text{shift}}\left(x, y\right) = I\left(x, y\right) g\left(x, y\right). \tag{17}$$

Assuming that the wavenumber spectrum center is shifted to the origin of the wavenumber domain, the phase expression should satisfy

$$\begin{cases} \frac{\partial\phi(x,y)}{\partial x} = -K_{xc} \\ \frac{\partial\phi(x,y)}{\partial y} = -K_{yc} \end{cases}. \tag{18}$$

Combining (15) and (18), the phase function $\phi(x, y)$ can be derived as

$$\phi\left(x, y\right) = -\frac{2\pi}{\lambda}\left[R_{\text{tr}}\left(0; x, y\right) + R_{\text{re},e}\left(x, y\right)\right] \tag{19}$$

where $R_{\text{re},e}(x, y)$ is the equivalent receiving range

$$R_{\text{re},e}\left(x, y\right) = \frac{1}{2}\left[R_{\text{re},1}\left(x, y\right) + R_{\text{re},2}\left(x, y\right)\right] \tag{20}$$

and the constant phase is ignored. The process of spectrum gap alignment is illustrated in Fig. 5. Imaging can then be implemented by filling the spectrum gap in each range bin.

IV. Imaging Method for Multistatic GEO SAR With Two Stationary Receivers

The proposed imaging algorithm for multistatic GEO SAR with two stationary receivers is introduced in this section.

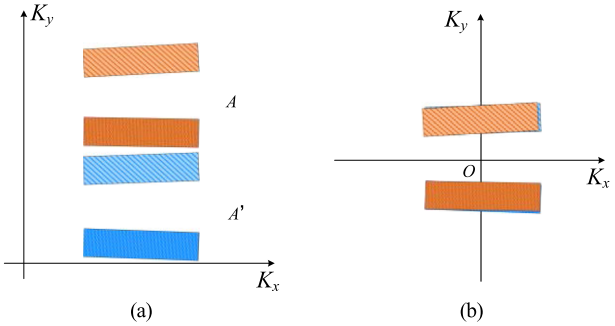

Fig. 5. Illustration of multistatic SAR wavenumber spectrum support of two point targets A and A' (a) before and (b) after spectrum gap alignment. The spectra of different targets are distinguished by color, whereas the different patterns correspond to signals received by different receivers.

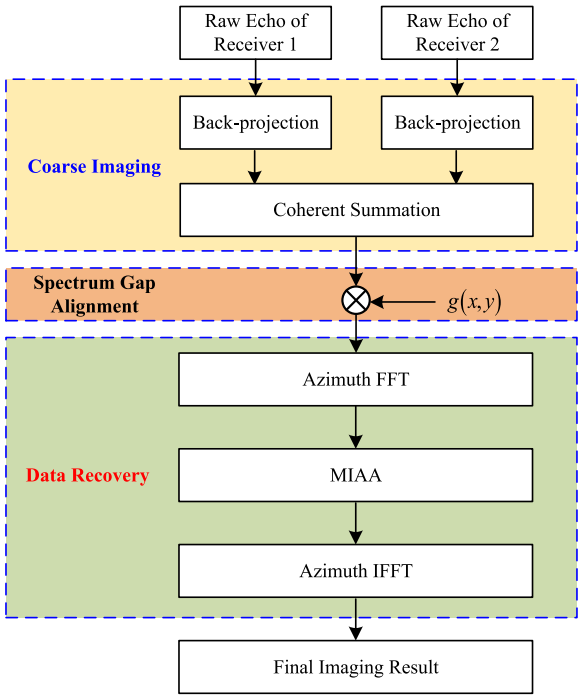

Fig. 6. Flowchart of the proposed imaging method for multistatic GEO SAR with two stationary receivers.

The algorithm contains three steps, namely coarse imaging, wavenumber spectrum gap alignment, and data recovery, as shown in Fig. 6.

A. Coarse Imaging

The ground plane imaging coordinate is the same as that in Section II.

Ground plane backprojection imaging [26] is first performed using the echo data of the two receivers, which can be modeled as

$$I_k(x,y) = \int_{T_s} s_{rc}\left(\frac{R_{\mathrm{bi},k}(t;x,y)}{c}, t\right) \exp\left\{j\frac{2\pi R_{\mathrm{bi},k}(t;x,y)}{\lambda}\right\} dt \tag{21}$$

where $I_k(x,y)$ represents the value of the imaging results at (x,y), $s_{rc}(\tau,t)$ is the range compressed data at fast time τ and slow time t, and $R_{\mathrm{bi},k}(t;x,y)$ is the bistatic range of the coordinate (x,y), which is calculated by

$$R_{\mathrm{bi},k}(t;x,y) = R_{\mathrm{tr}}(t;x,y) + R_{\mathrm{re},k}(x,y). \tag{22}$$

Gridding is implemented along the *X* and *Y* directions, and the same imaging grids are used for both receivers.

Then, the coarse imaging results $I_1(x,y)$ and $I_2(x,y)$ are coherently combined

$$I(x,y) = I_1(x,y) + I_2(x,y) \tag{23}$$

and wavenumber spectrum gap is aligned using the method described in Section III.

B. Data Recovery

After the spectrum gap alignment is completed, the image is transformed into an azimuth wavenumber domain via fast Fourier transform (FFT) along the azimuth direction. The wavenumber domain signal in each range bin is modeled as

$$S_a(K_y) = W_a(K_y)\exp(-jK_y y_0) \tag{24}$$

where $W_a(K_y)$ is the envelope and can be represented by

$$W_a(K_y) = \begin{cases} 1 & \left|K_y - \frac{K_{yc,1}-K_{yc,2}}{2}\right| \le \frac{B_1}{2} \\ & \left|K_y - \frac{K_{yc,2}-K_{yc,1}}{2}\right| \le \frac{B_2}{2} \\ 0 & \text{else} \end{cases}. \tag{25}$$

The spectrum with a gap in the middle can be considered as a uniformly sampled signal with missing data. To recover the full spectrum, the missing-data iterative adaptive approach (MIAA) [27], [28], [29] is applied here. The spectrum signal is truncated such that the wavenumber below

$$K_{\mathrm{lower}} = \frac{K_{yc,2}-K_{yc,1}}{2} - \frac{B_2}{2} \tag{26}$$

and beyond

$$K_{\mathrm{upper}} = \frac{K_{yc,1}-K_{yc,2}}{2} + \frac{B_1}{2} \tag{27}$$

are discarded.

Let

$$\begin{aligned} \mathbf{s} &\triangleq \left[s(0) \quad s(1) \quad \cdots \quad s(N-1)\right]^{\mathrm{T}} \\ &\triangleq \left[\mathbf{s}_1^{\mathrm{T}} \quad \mathbf{s}_2^{\mathrm{T}} \quad \mathbf{s}_3^{\mathrm{T}}\right]^{\mathrm{T}} \end{aligned} \tag{28}$$

be the truncated wavenumber domain signal in an arbitrary range gate, where *N* is the vector length, $\mathbf{s}_1$ and $\mathbf{s}_3$ are the signal in the support region of $W_a(K_y)$ whose length are N_1 and N_3, respectively, and $\mathbf{s}_2$ is the data gap whose length is $N_2 = N - N_1 - N_3$. The data vector $\mathbf{s}$ can be modeled as

$$\mathbf{s} = \mathbf{A}\boldsymbol{\alpha} \tag{29}$$

where $\mathbf{A}=[\mathbf{a}(\omega_0),\mathbf{a}(\omega_1),\ldots,\mathbf{a}(\omega_{Q-1})]$ is the inverse Fourier transform matrix,

$$\mathbf{a}(\omega_q)=[1,\exp(j\omega_q),\exp(j2\omega_q),\ldots,\exp(j(N-1)\omega_q)]^{\mathrm{T}}$$
$$q=0,1,\ldots,Q-1 \tag{30}$$

is the column vector of $\mathbf{A}$, $\omega_q=2\pi q/N$ is the frequency point, and Q is the number of frequency grid points. $\boldsymbol{\alpha}=[\alpha_0,\alpha_1,\ldots,\alpha_{Q-1}]^{\mathrm{T}}$ is the complex spectral amplitude vector.

MIAA estimates the complex spectral amplitude of each frequency grid point by minimizing the interference of the rest of the frequency grids. The elements of $\boldsymbol{\alpha}$ can be iteratively solved using

$$\alpha_q=\frac{\mathbf{a}_g^H(\omega_q)\mathbf{R}_g^{-1}\mathbf{s}_g}{\mathbf{a}_g^H(\omega_q)\mathbf{R}_g^{-1}\mathbf{a}_g(\omega_q)} \tag{31}$$

where

$$\mathbf{a}_g(\omega_q)=\left[\mathbf{a}_1^{\mathrm{T}}(\omega_q),\mathbf{a}_3^{\mathrm{T}}(\omega_q)\right]^{\mathrm{T}} \tag{32}$$

$$\mathbf{a}_1(\omega_q)=\begin{bmatrix}1\\ \exp(j\omega_q)\\ \exp(j2\omega_q)\\ \cdots\\ \exp(j(N_1-1)\omega_q)\end{bmatrix} \tag{33}$$

$$\mathbf{a}_3(\omega_q)=\begin{bmatrix}\exp(j(N_1+N_2)\omega_q)\\ \exp(j(N_1+N_2+1)\omega_q)\\ \cdots\\ \exp(j(N-1)\omega_q)\end{bmatrix} \tag{34}$$

$$\mathbf{R}_g=\sum_{q=0}^{Q-1}|\alpha_q|^2\mathbf{a}_g(\omega_q)\mathbf{a}_g^{\mathrm{H}}(\omega_q) \tag{35}$$

$$\mathbf{s}_g=\left[\mathbf{s}_1^{\mathrm{T}}\quad\mathbf{s}_3^{\mathrm{T}}\right]^{\mathrm{T}} \tag{36}$$

and $(\cdot)^{\mathrm{H}}$ represents the conjugate transpose operator.

Then, the data gap can be estimated by

$$\mathbf{s}_2=\sum_{q=0}^{Q-1}|\alpha_q|^2\mathbf{a}_2(\omega_q)\mathbf{a}_g^{\mathrm{H}}(\omega_q)\mathbf{R}_g^{-1}\mathbf{s}_g \tag{37}$$

where

$$\mathbf{a}_2(\omega_q)=\begin{bmatrix}\exp(jN_1\omega_q)\\ \exp(j(N_1+1)\omega_q)\\ \cdots\\ \exp(j(N_1+N_2-1)\omega_q)\end{bmatrix}. \tag{38}$$

After implementing MIAA in each range bin, the spectrum gap in the azimuth wavenumber domain is filled, and the final imaging result can be obtained via inverse fast Fourier transform along the azimuth direction.

V. Simulation and Results

The proposed method is validated in this section through simulation. A simulation scene that covers 1 km × 1 km and consists of eight point targets with identical radar cross section is illustrated in Fig. 7. Three point pairs with azimuth space of 10 m are located at the lower left corner, the scene center, and the upper right corner, respectively. Two points are distributed at the upper left corner and lower right corner, respectively. The system parameters are listed in Table I and the synthetic aperture time is 352 s.

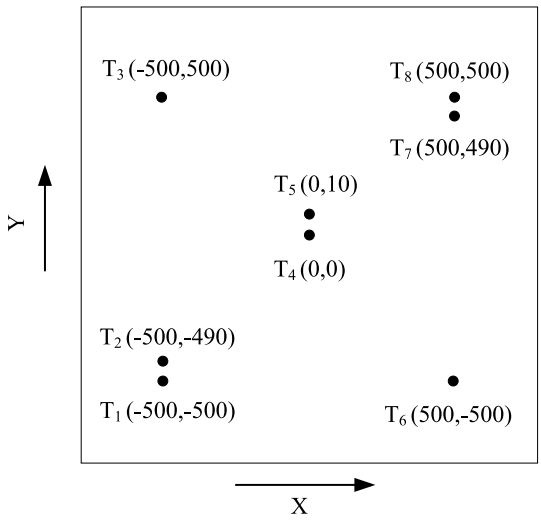

Fig. 7. Simulation scene covering an area of 1 km × 1 km.

TABLE II
Evaluation of Point Target Imaging Results

Point	Resolution (m)		PSLR (dB)		ISLR (dB)	
	Range	Azimuth	Range	Azimuth	Range	Azimuth
T_3	2.99	2.89	-14.44	-12.63	-12.80	-9.66
T_6	2.80	3.14	-15.42	-12.38	-14.00	-9.52

The 2-D wavenumber domain before spectrum gap alignment is illustrated in Fig. 8(a). The spectrum gaps of different targets cannot be recognized since the spectrum support region covers the whole azimuth bandwidth. The result of spectrum gap alignment is shown in Fig. 8(b). As can be seen, the spectra of different receivers are separated, and the spectrum gaps are centered at the origin of the wavenumber domain, which verifies the effectiveness of the proposed gap alignment method. The spectrum result of the final image is shown in Fig. 8(c) where the area between the support regions in Fig. 8(b) is filled with data, which indicates that the data are recovered, achieving full spectrums.

The range and azimuth profiles of the imaging results of point target T_3 and T_6 are shown in Fig. 9. The imaging quality is evaluated by resolution, peak sidelobe ratio (PSLR), and integrated sidelobe ratio (ISLR), and the results are listed in Table II. The azimuth profiles are close to sinc functions and the peak sidelobe levels are around −12 dB, which indicates that the azimuth spectrum shape after data recovery is close to a rectangle.

To verify the performance of the proposed imaging method against noise, another simulation is implemented where the signal-to-noise ratio (SNR) of the echo in the 2-D time domain is set as −30 dB, which corresponds to SNR of 9 dB in the azimuth wavenumber domain. Three imaging methods, namely coherent

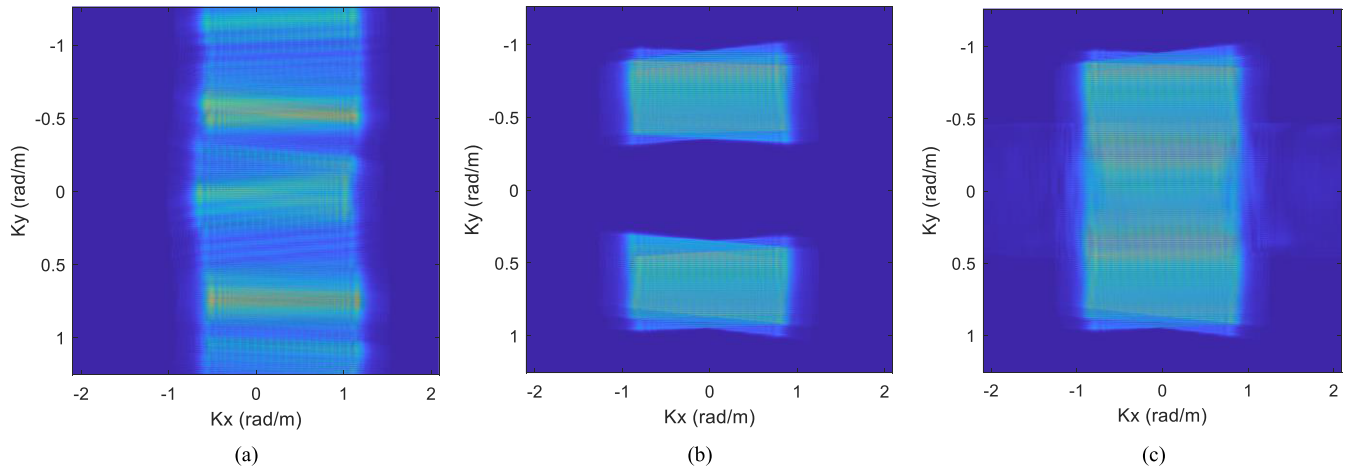

Fig. 8. Illustration of 2-D wavenumber domain (a) before spectrum gap alignment, (b) after spectrum alignment, and (c) after data recovery.

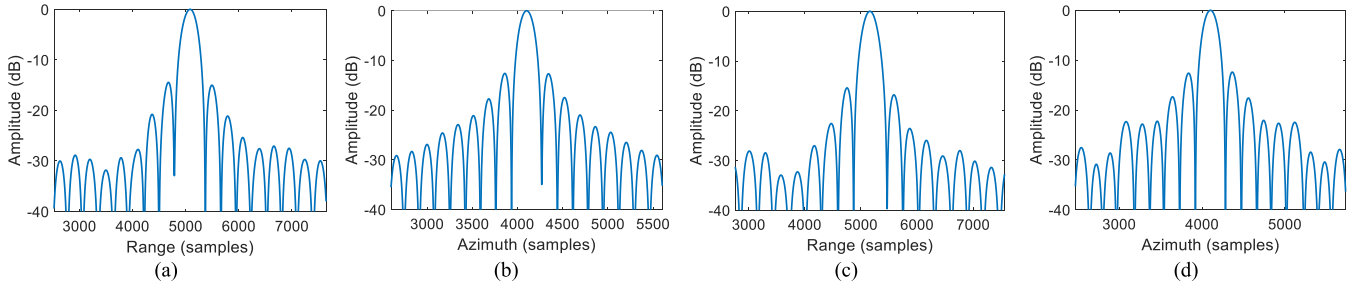

Fig. 9. Imaging results of the proposed method. (a) and (c) Range profiles of T3 and T6. (b) and (d) Azimuth profiles of T3 and T6.

TABLE III
SIDELOBE LEVEL OF ADJACENT POINT TARGETS

	T_1 and T_2	T_4 and T_5	T_7 and T_8
Coherent combination	0.07 (dB)	1.19 (dB)	0.60 (dB)
SAE	-3.11 (dB)	-1.12 (dB)	-1.35 (dB)
Proposed method	-10.05 (dB)	-7.03 (dB)	-4.31 (dB)

TABLE IV
RESOLUTION OF ADJACENT POINT TARGETS

Point	Coherent combination		SAE		Proposed method	
	Range	Azimuth	Range	Azimuth	Range	Azimuth
T1	3.06	2.34	3.20	2.66	2.77	2.99
T2	2.96	2.36	2.82	2.91	2.61	2.93
T4	3.00	2.44	2.91	2.85	2.94	3.03
T5	2.99	2.42	2.94	2.77	3.12	2.97
T7	3.01	2.56	2.87	3.03	2.21	2.97
T8	2.95	2.54	2.54	3.22	2.13	3.16

combination [18], spectrum alignment and extrapolation (SAE) [16], and the proposed method are used.

The azimuth profiles of the point pairs are shown in Fig. 10, where the arrows in the figures point to the main lobes of the point targets. Define local PSLR as the larger PSLR of the two adjacent points. As shown in Table III, the sidelobe levels are close to those of the main lobes when implementing the coherent combination method, which means the artifacts caused by the sidelobes may be observed in the imaging results.

Compared to SAE, the proposed method can achieve lower local PSLR, leading to better imaging performance considering the azimuth sidelobe level. The resolutions of adjacent point targets are evaluated and listed in Table IV. The proposed method basically preserves the range resolution compared to the coherent combination method, whereas the azimuth resolution is approximately 3 m, which is consistent with the theoretical value. Considering both resolution and sidelobe level comprehensively, the proposed method has better imaging performance.

To further demonstrate the superiority of the proposed method, an extended target simulation based on a TerraSAR-X image is implemented. The image shown in Fig. 11(a) covers an area of 1 km $\times$ 1 km and the width between adjacent pixels in range and azimuth direction is 3 m. The value of each pixel is regarded as the backscattering coefficient, and the echo data can be simulated using the parameters listed in Table I. The imaging results using the coherent combination, SAE, and the proposed method are shown in Fig. 11(b)–(d). It is illustrated in Fig. 11(e) and (f) that the imaging results of the strong scattering centers achieved by the proposed method have the lowest azimuth

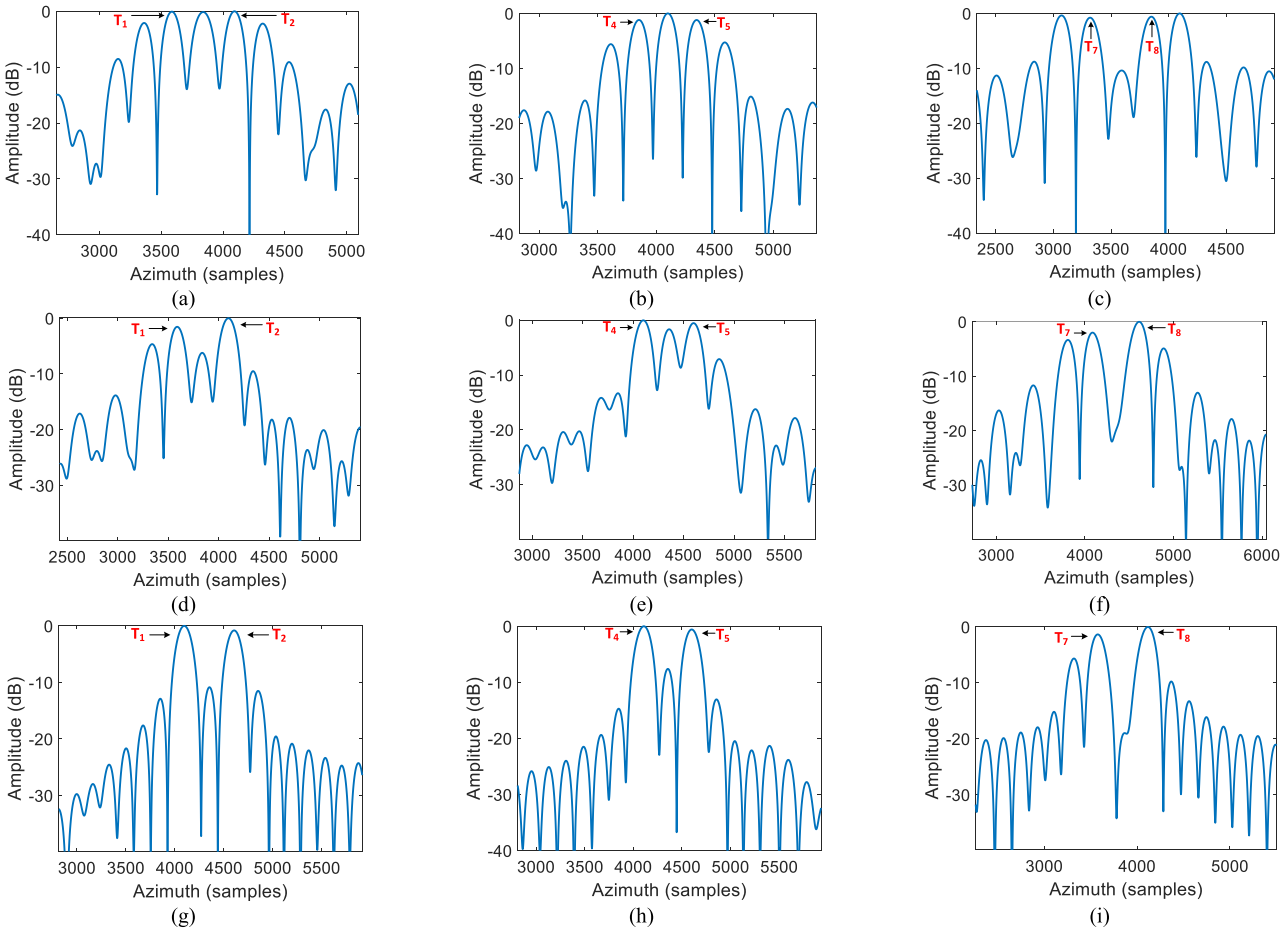

Fig. 10. Azimuth profiles of adjacent points achieved by coherent combination, SAE, and the proposed method. (a)–(c) Results achieved by coherent combination. (d)–(f) Results achieved by SAE. (g)–(i) Results achieved by the proposed method.

sidelobes, which indicates better imaging performance over the other two methods.

VI. Discussion

A. Computational Load

As mentioned in Section IV, the proposed algorithm consists of coarse imaging, wavenumber spectrum gap alignment, and data recovery. Assume that the echo data size is N_a and N_r in azimuth and range direction, respectively, and the size of the imaging area is $N_r \times N_r$. The computational load of coarse imaging is [16]

$$C_1 = (10M_0 + 10) N_a N_r \log_2 (N_r) + [10M_0 \log_2 (M_0) + 12] N_a N_r + 16 N_a N_r^2 + 2N_r^2 \tag{39}$$

where M_0 is the interpolator length. Spectrum gap alignment requires one complex multiplication for each pixel, and the computational load is $C_2 = 6N_r^2$. Suppose the spectrum gap length is $N_r/2$ and the frequency grid point number is $Q = 4N_r$. The computational load of data recovery is approximately $114N_r^4$, which occupies a majority of workloads since matrix inversion and iteration are included.

In the extended target simulation, the CPU and processing software are Intel Xeon W-10855M and MATLAB R2017a. The computing times in the experiment are 119.2, 138.8, and 177.2 s for coherent combination, SAE, and the proposed method, respectively. The results show that the proposed method improves the azimuth imaging performance at the cost of computation, which is worthwhile considering suppressing the artifacts in the final image.

B. Influence of Target Elevation

The proposed method uses the backprojection method for coarse imaging, where the imaging plane is set as the ground plane. When the height of a target is not zero, phase error will occur in the imaging results [30]. To further analyze the influence of target's height on the imaging results, a point target, whose X and Y coordinates are 500 and -500 m, respectively, with different heights is simulated using the parameters in Table I.

Fig. 12(a) and (b) shows the range and azimuth profile of a point target located at (500 m, -500 m, 500 m). It is illustrated that the azimuth sidelobe level is higher than -13 dB. Table V

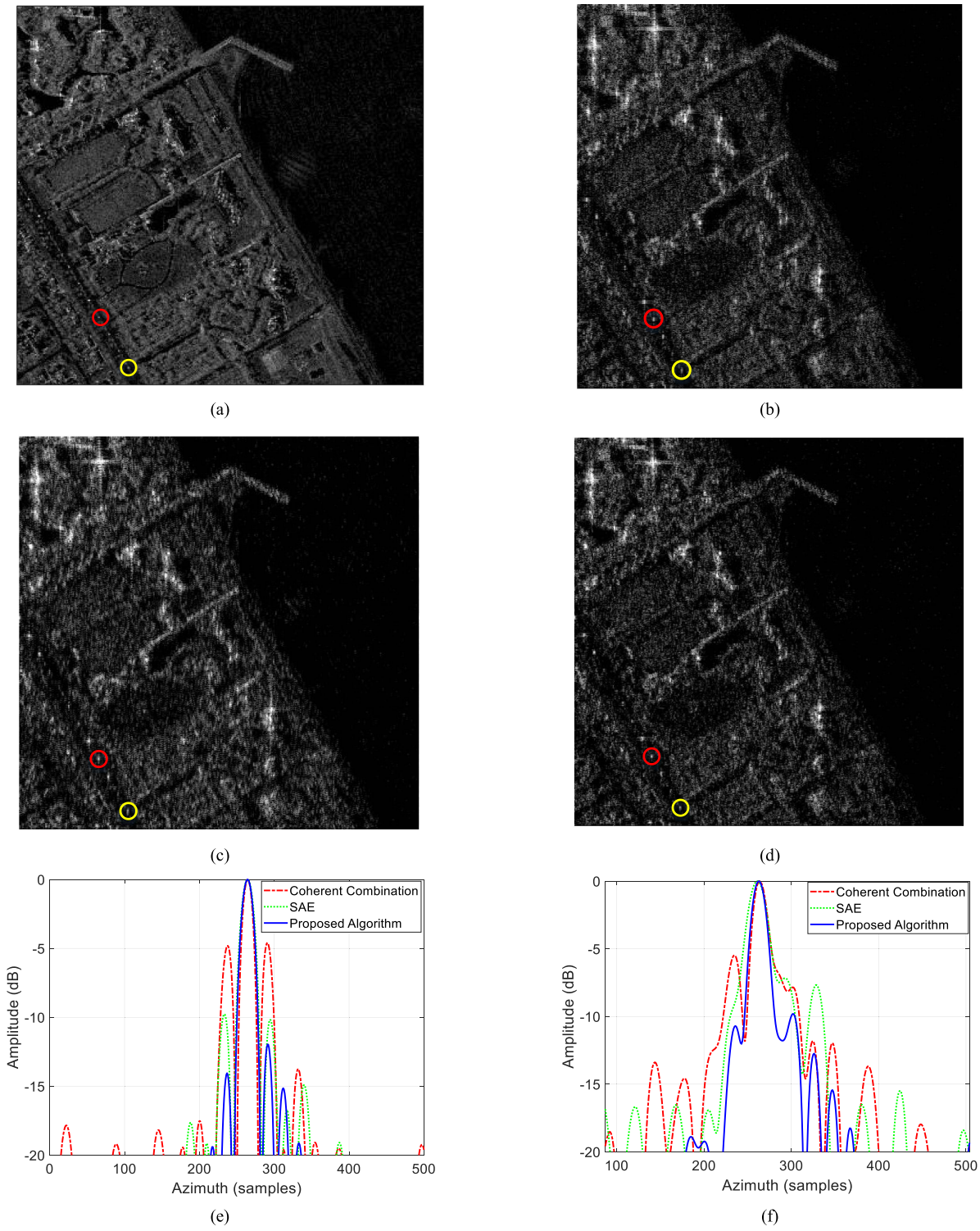

Fig. 11. Imaging results of the extended target simulation. (a) Original TerraSAR-X image. (b)–(d) Results achieved by coherent combination, SAE, and the proposed method, respectively. (e) and (f) Azimuth profiles of the targets in the red and yellow circles, respectively.

gives the azimuth PSLR result with different target heights. It is indicated that the performance of spectrum gap recovery is not satisfactory. This is probably because MIAA is more accurate in estimating linear phases when recovering spectral gaps. When phase error of second or higher order exists, it will introduce error in both amplitude and phase, which causes a high sidelobe level.

Better imaging performance may be achieved by compensating for the phase error after BP imaging and after spectrum gap recovery. The imaging result of the point target at (500 m,

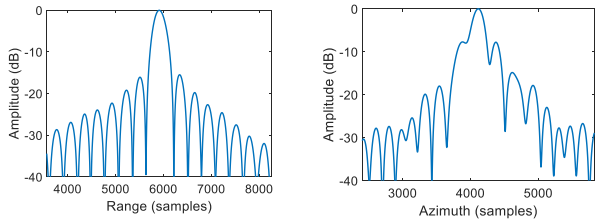

(a) (b)

Fig. 12. Imaging performance of a point target located at (500 m, −500 m, 500 m). (a) Range profile. (b) Azimuth profile.

TABLE V
AZIMUTH PSLR WITH DIFFERENT HEIGHT

Height	0	100	200	300	400	500	600	700
PSLR	-12.40	-2.65	-11.74	-4.90	-8.86	-7.74	-2.18	-4.79

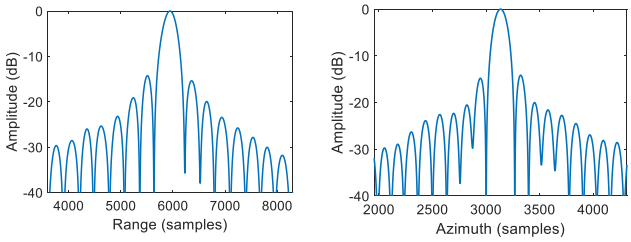

(a) (b)

Fig. 13. Imaging performance combining the proposed method and phase compensation. (a) Range profile. (b) Azimuth profile.

−500 m, 500 m) after compensating for the phase error using phase gradient autofocus is shown in Fig. 13. Compared to Fig. 12, the azimuth sidelobe is lower, which infers that the proposed method can be used with phase compensation to focus targets with nonzero height.

VII. CONCLUSION

This article proposes an imaging method for multistatic GEO SAR with two stationary receivers. The spectrum gaps are aligned for all the targets in the scene, and the full spectrum is recovered, resulting in fine azimuth imaging performance. Results of point target and extended target simulation verify that the proposed method can achieve lower sidelobe levels compared to existing methods. Further studies will include the applicability of the method when focusing multistatic SAR with single-input–multiple-output [31] and multiple-input–multiple-output configurations [32], [33], [34] as well as tomographic imaging [35].

APPENDIX A

According to (5), the azimuth ambiguity function can be expressed as

$$\begin{aligned}
&\chi\left(\mathbf{r}_A,\mathbf{r}_B\right)\\
&=\frac{1}{2}\mathrm{sinc}\left[T_s\boldsymbol{\Gamma}_g^T\left(\mathbf{r}_B-\mathbf{r}_A\right)\right]\times\sum_{k=1}^{2}\exp\left[j\frac{2\pi}{\lambda}\mathbf{u}_{g,k}^T\left(\mathbf{r}_B-\mathbf{r}_A\right)\right]\\
&=\mathrm{sinc}\left[T_s\boldsymbol{\Gamma}_g^T\left(\mathbf{r}_B-\mathbf{r}_A\right)\right]\\
&\quad\times\exp\left\{j\frac{2\pi}{\lambda}\frac{\left(\mathbf{u}_{g,1}+\mathbf{u}_{g,2}\right)^T}{2}\left(\mathbf{r}_B-\mathbf{r}_A\right)\right\}\\
&\quad\times\cos\left[\frac{\pi(\mathbf{u}_{g,1}-\mathbf{u}_{g,2})^T}{\lambda}\left(\mathbf{r}_B-\mathbf{r}_A\right)\right] \qquad \text{(A1)}
\end{aligned}$$

where $\mathbf{u}_{g,k}$ is the ground projection of the bistatic range gradient vector given by

$$\mathbf{u}_{g,k}=\left(\mathbf{I}-\mathbf{u}_z\mathbf{u}_z^T\right)\left(\mathbf{u}_{TA}+\mathbf{u}_{RA,k}\right) \qquad \text{(A2)}$$

where $\mathbf{I}$ is a third order unit matrix, $\mathbf{u}_z=[0,0,1]^T$ is the unit vector of the z-direction, and $\mathbf{u}_{TA}$ and $\mathbf{u}_{RA,k}$ are the unit vectors along the transmitting range and receiving range at the aperture center, respectively, pointing to the target A.

When the two receiving ranges of the receivers are approximately equal, it can be derived that

$$\begin{aligned}
\frac{\mathbf{u}_{g,1}+\mathbf{u}_{g,2}}{2}&=\left(I-\mathbf{u}_z\mathbf{u}_z^T\right)\left(\mathbf{u}_{TA}+\frac{\mathbf{u}_{RA,1}+\mathbf{u}_{RA,2}}{2}\right)\\
&\approx\left(I-\mathbf{u}_z\mathbf{u}_z^T\right)\left(\mathbf{u}_{TA}+\frac{\mathbf{r}_{\mathrm{re},M}}{R_{\mathrm{re},M}}\right)\\
&=\mathbf{u}_{g,M} \qquad \text{(A3)}
\end{aligned}$$

where $\mathbf{u}_{g,M}$ is the ground projection of the bistatic range gradient vector of the equivalent system. When the scene is far from the receivers, it can be derived that

$$\begin{aligned}
\mathbf{u}_{g,1}-\mathbf{u}_{g,2}&=\left(I-\mathbf{u}_z\mathbf{u}_z^T\right)\left(\mathbf{u}_{RA,1}-\mathbf{u}_{RA,2}\right)\\
&=\frac{\mathbf{r}_{RA,M}+\frac{\mathbf{d}}{2}}{R_{\mathrm{re},1}}-\frac{\mathbf{r}_{RA,M}-\frac{\mathbf{d}}{2}}{R_{\mathrm{re},2}}\\
&\approx\frac{\mathbf{r}_{RA,M}+\frac{\mathbf{d}}{2}}{R_{\mathrm{re},M}}-\frac{\mathbf{r}_{RA,M}-\frac{\mathbf{d}}{2}}{R_{\mathrm{re},M}}\\
&=\frac{\mathbf{d}}{R_{\mathrm{re},M}} \qquad \text{(A4)}
\end{aligned}$$

where $\mathbf{d}=\mathbf{r}_{RA,1}-\mathbf{r}_{RA,2}$ is the vector pointing from receiver 1 to receiver 2.

Applying (A1) to (A3) and (A4) yields

$$\begin{aligned}
&\chi\left(\mathbf{r}_A,\mathbf{r}_B\right)\\
&=\frac{1}{2}\mathrm{sinc}\left[T_s\boldsymbol{\Gamma}_g^T\left(\mathbf{r}_B-\mathbf{r}_A\right)\right]\times\sum_{k=1}^{2}\exp\left[j\frac{2\pi}{\lambda}\mathbf{u}_{g,k}^T\left(\mathbf{r}_B-\mathbf{r}_A\right)\right]\\
&=\mathrm{sinc}\left[T_s\boldsymbol{\Gamma}_g^T\left(\mathbf{r}_B-\mathbf{r}_A\right)\right]\exp\left\{j\frac{2\pi}{\lambda}\mathbf{u}_{g,M}^T\left(\mathbf{r}_B-\mathbf{r}_A\right)\right\}\\
&\quad\times\cos\left[\frac{\pi}{\lambda R_{re,M}}\mathbf{d}^T\left(\mathbf{r}_B-\mathbf{r}_A\right)\right]. \qquad \text{(A5)}
\end{aligned}$$

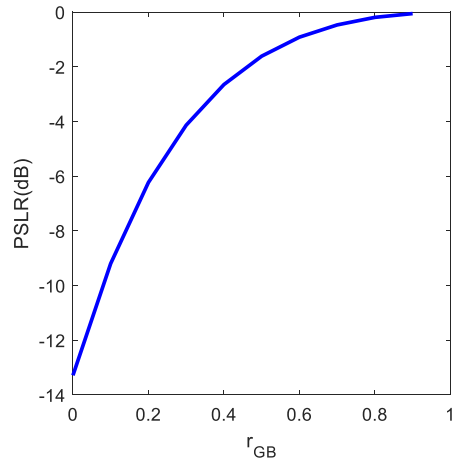

Fig. 14. Azimuth PSLR variation with r_{GB}.

Appendix B

The azimuth ambiguity function can be expressed as

$$\chi\left(\mathbf{r}_B-\mathbf{r}_A\right)=\operatorname{sinc}\left[T_s\boldsymbol{\Gamma}_g^T\left(\mathbf{r}_B-\mathbf{r}_A\right)\right]\cos\left[\frac{\pi}{\lambda R_{re,M}}\mathbf{d}^T\left(\mathbf{r}_B-\mathbf{r}_A\right)\right]. \tag{A6}$$

Assume that the Doppler gradient is perpendicular to the Y direction, and the two receivers are aligned along the Y direction. The azimuth ambiguity function can be simplified as

$$\chi\left(y\right)=\operatorname{sinc}\left[\frac{\Delta K y}{2\pi}\right]\cos\left[K_1 y\right] \tag{A7}$$

where

$$\begin{cases}\Delta K=2\pi T_s\left\|\boldsymbol{\Gamma}_g\right\|\\ K_1=\frac{\|\mathbf{d}\|\pi}{\lambda R_{\mathrm{re},M}}\end{cases}. \tag{A8}$$

By performing FFT, (A7) is transformed to the wavenumber domain, which yields

$$X\left(K_y\right)=\operatorname{rect}\left[\frac{K_y+K_1}{\Delta K}\right]+\operatorname{rect}\left[\frac{K_y-K_1}{\Delta K}\right]. \tag{A9}$$

The ratio between the spectrum gap and the total bandwidth can be calculated as

$$r_{\mathrm{GB}}=\frac{2K_1-\Delta K}{2K_1+\Delta K}. \tag{A10}$$

The PSLR corresponding to r_{GB} is demonstrated in Fig. 14. It can be inferred that when the spectrum gap exists, the PSLR is higher than -13 dB.

References

[1] K. Tomiyasu and J. L. Pacelli, "Synthetic aperture radar imaging from an inclined geosynchronous orbit," *IEEE Trans. Geosci. Remote Sens.*, vol. GE-21, no. 3, pp. 324–329, Jul. 1983.

[2] S. Hobbs, C. Mitchell, B. Forte, R. Holley, B. Snapir, and P. Whittaker, "System design for geosynchronous synthetic aperture radar missions," *IEEE Trans. Geosci. Remote Sens.*, vol. 52, no. 12, pp. 7750–7763, Dec. 2014.

[3] D. Bruno and S. E. Hobbs, "Radar imaging from geosynchronous orbit: Temporal decorrelation aspects," *IEEE Trans. Geosci. Remote Sens.*, vol. 48, no. 7, pp. 2924–2929, Jul. 2010.

[4] J. Ruiz-Rodon, A. Broquetas, E. Makhoul, A. M. Guarnieri, and F. Rocca, "Nearly zero inclination geosynchronous SAR mission analysis with long integration time for earth observation," *IEEE Trans. Geosci. Remote Sens.*, vol. 52, no. 10, pp. 6379–6391, Oct. 2014, doi: 10.1109/TGRS.2013.2296357.

[5] J. Chen et al., "A parameter optimization model for geosynchronous SAR sensor in aspects of signal bandwidth and integration time," *IEEE Geosci. Remote Sens. Lett.*, vol. 13, no. 9, pp. 1374–1378, Sep. 2016, doi: 10.1109/LGRS.2016.2587318.

[6] Z. Ding, W. Yin, T. Zeng, and T. Long, "Radar parameter design for geosynchronous SAR in squint mode and elliptical orbit," *IEEE J. Sel. Topics Appl. Earth Observ. Remote Sens.*, vol. 9, no. 6, pp. 2720–2732, Jun. 2016, doi: 10.1109/JSTARS.2016.2570231.

[7] A. Recchia, A. M. Guarnieri, A. Broquetas, and A. Leanza, "Impact of scene decorrelation on geosynchronous SAR data focusing," *IEEE Trans. Geosci. Remote Sens.*, vol. 54, no. 3, pp. 1635–1646, Mar. 2016, doi: 10.1109/TGRS.2015.2486385.

[8] J. Geng, Z. Yu, C. Li, and W. Liu, "Squint mode GEO SAR imaging using bulk range walk correction on received signals," *Remote Sens.*, vol. 11, no. 1, Dec. 2018, Art. no. 17, doi: 10.3390/rs11010017.

[9] F. Chang, D. Li, Z. Dong, Y. Huang, Z. He, and X. Chen, "Elevation spatial variation analysis and compensation in GEO SAR imaging," *Remote Sens.*, vol. 13, no. 10, May 2021, Art. no. 1888, doi: 10.3390/rs13101888.

[10] J. Nicolás-Álvarez et al., "Interferometric orbit determination system for geosynchronous SAR missions: Experimental proof of concept," *Remote Sens.*, vol. 14, no. 19, Sep. 2022, Art. no. 4871, doi: 10.3390/rs14194871.

[11] F. Chang, C. Yu, D. Li, Y. Ji, and Z. Dong, "An accurate Doppler parameters calculation method of geosynchronous SAR considering real-time zero-doppler centroid control," *Remote Sens.*, vol. 13, no. 20, Oct. 2021, Art. no. 4061, doi: 10.3390/rs13204061.

[12] B. Zhou, X. Qi, and H. Zhang, "An accurate GEO SAR range model for ultralong integration time based on *m*th-order Taylor expansion," *Remote Sens.*, vol. 13, no. 2, Jan. 2021, Art. no. 255, doi: 10.3390/rs13020255.

[13] D. Li, X. Zhu, Z. Dong, A. Yu, and Y. Zhang, "Background tropospheric delay in geosynchronous synthetic aperture radar," *Remote Sens.*, vol. 12, no. 18, Sep. 2020, Art. no. 3081, doi: 10.3390/rs12183081.

[14] C. Hu, Y. Li, X. Dong, C. Cui, and T. Long, "Impacts of temporal-spatial variant background ionosphere on repeat-track GEO D-InSAR system," *Remote Sens.*, vol. 8, no. 11, Nov. 2016, Art. no. 916, doi: 10.3390/rs8110916.

[15] H. Nies, F. Behner, S. Reuter, and O. Loffeld, "First results of passive radar imaging and tracking using geostationary satellites," in *Proc. 15th Eur. Radar Conf.*, 2018, pp. 214–217, doi: 10.23919/EuRAD.2018.8546511.

[16] Y. Guo, Z. Yu, J. Li, and C. Li, "Focusing multistatic GEO SAR with two stationary receivers using spectrum alignment and extrapolation," *IEEE Geosci. Remote Sens. Lett.*, vol. 19, 2022, Art. no. 4018805, doi: 10.1109/LGRS.2021.3111763.

[17] C. Yang, T. Zeng, and Z. Ding, "A high resolution multiple-receiver SS-BSAR system," in *Proc. IET. Int. Radar Conf.*, 2009, pp. 1–5, doi: 10.1049/cp.2009.0102.

[18] F. Santi, G. P. Blasone, D. Pastina, F. Colone, and P. Lombardo, "Parasitic surveillance potentialities based on a GEO-SAR illuminator," *Remote Sens.*, vol. 13, no. 23, Nov. 2021, Art. no. 4817, doi: 10.3390/rs13234817.

[19] X. Su, L. Dongying, S. Ye, Y. Ma, Z. Cui, and S. Ouyang, "Structure design and thermal deformation simulation of spaceborne SAR antenna," in *Proc. 2nd China Int. SAR Symp.*, 2021, pp. 1–4, doi: 10.23919/CISS51089.2021.9652209.

[20] Y. Kim and R. L. Jordan, "Spaceborne SAR antennas for earth science," in *Spaceborne Antennas for Planetary Exploration*, W. A. Imbriale, Ed. Hoboken, NJ, USA: Wiley, 2006, pp. 305–340, doi: 10.1002/0470052783.ch6.

[21] U. Nithirochananont, M. Antoniou, and M. Cherniakov, "Passive coherent multistatic SAR using spaceborne illuminators," *IET Radar, Sonar Navigat.*, vol. 14, no. 4, pp. 628–636, Apr. 2020, doi: 10.1049/iet-rsn.2019.0425.

[22] E. G. Larsson, G. Liu, P. Stoica, and J. Li, "High-resolution SAR imaging with angular diversity," *IEEE Trans. Aerosp. Electron. Syst.*, vol. 37, no. 4, pp. 1359–1372, Oct. 2001, doi: 10.1109/7.976971.

[23] T. Zeng, M. Cherniakov, and T. Long, "Generalized approach to resolution analysis in BSAR," *IEEE Trans. Aerosp. Electron. Syst.*, vol. 41, no. 2, pp. 461–474, Apr. 2005, doi: 10.1109/TAES.2005.1468741.

[24] X. Chen, G.-C. Sun, M. Xing, B. Li, J. Yang, and Z. Bao, "Ground cartesian back-projection algorithm for high squint diving TOPS SAR imaging," *IEEE Trans. Geosci. Remote Sens.*, vol. 59, no. 7, pp. 5812–5827, Jul. 2021, doi: 10.1109/TGRS.2020.3011589.
[25] H. Zhang et al., "Spaceborne/stationary bistatic SAR imaging with TerraSAR-X as an illuminator in staring-spotlight mode," *IEEE Trans. Geosci. Remote Sens.*, vol. 54, no. 9, pp. 5203–5216, Sep. 2016, doi: 10.1109/TGRS.2016.2558294.
[26] Q. Dong, G.-C. Sun, Z. Yang, L. Guo, and M. Xing, "Cartesian factorized backprojection algorithm for high-resolution spotlight SAR imaging," *IEEE Sensors J.*, vol. 18, no. 3, pp. 1160–1168, Feb. 2018, doi: 10.1109/JSEN.2017.2780164.
[27] P. Stoica, J. Li, and J. Ling, "Missing data recovery via a nonparametric iterative adaptive approach," *IEEE Signal Process. Lett.*, vol. 16, no. 4, pp. 241–244, Apr. 2009, doi: 10.1109/LSP.2009.2014114.
[28] J. Karlsson, W. Rowe, L. Xu, G.-O. Glentis, and J. Li, "Fast missing-data IAA with application to notched spectrum SAR," *IEEE Trans. Aerosp. Electron. Syst.*, vol. 50, no. 2, pp. 959–971, Apr. 2014, doi: 10.1109/TAES.2014.120529.
[29] X. Wang, R. Wang, Y. Deng, W. Wang, and N. Li, "SAR signal recovery and reconstruction in staggered mode with low oversampling factors," *IEEE Geosci. Remote Sens. Lett.*, vol. 15, no. 5, pp. 704–708, May 2018, doi: 10.1109/LGRS.2018.2805311.
[30] Y. Guo, Z. Yu, J. Yu, J. Li, and X. Zhao, "Height estimation of strong scatterers for bistatic GEO SAR with a stationary receiver," in *Proc. IEEE Int. Geosci. Remote Sens. Symp.*, 2022, pp. 1840–1843, doi: 10.1109/IGARSS46834.2022.9884058.
[31] J. Mittermayer et al., "MirrorSAR: An HRWS add-on for single-pass multi-baseline SAR interferometry," *IEEE Trans. Geosci. Remote Sens.*, vol. 60, 2022, Art. no. 5224018, doi: 10.1109/TGRS.2021.3132384.
[32] C. Hu, Z. Chen, X. Dong, and C. Cui, "Multistatic geosynchronous SAR resolution analysis and grating lobe suppression based on array spatial ambiguity function," *IEEE Trans. Geosci. Remote Sens.*, vol. 58, no. 9, pp. 6020–6038, Sep. 2020, doi: 10.1109/TGRS.2020.2969573.
[33] A. M. Guarnieri et al., "ARGOS: A fractioned geosynchronous SAR," *Acta Astronautica*, vol. 164, pp. 444–457, Nov. 2019, doi: 10.1016/j.actaastro.2015.11.022.
[34] D. Giudici, P. Guccione, M. Manzoni, A. M. Guarnieri, and F. Rocca, "Compact and free-floating satellite MIMO SAR formations," *IEEE Trans. Geosci. Remote Sens.*, vol. 60, 2022, Art. no. 1000212, doi: 10.1109/TGRS.2021.3062973.
[35] Y. Wang et al., "First demonstration of single-pass distributed SAR tomographic imaging with a P-band UAV SAR prototype," *IEEE Trans. Geosci. Remote Sens.*, vol. 60, 2022, Art. no. 5238618, doi: 10.1109/TGRS.2022.3221859.

Yukun Guo was born in Beijing, China, in 1990. He received the B.S. degree in electronics engineering and the Ph.D. degree in signal and information processing from Beihang University, Beijing, China, in 2013 and 2022, respectively.

Since 2022, he has been a Postdoctoral Fellow with the School of Electronics and Information Engineering, Beihang University. His research interests include system design and signal processing for high-resolution multistatic synthetic aperture radar.

Ze Yu (Member, IEEE) was born in Xi'an, Shaanxi, China, in 1979. He received the B.S. degree in electronics engineering and the Ph.D. degree in communication and information systems from Beihang University, Beijing, China, in 2002 and 2007, respectively.

Since 2009, he has been with the School of Electronics and Information Engineering, Beihang University. His research interests include system design and imaging processing for high-resolution and wide-swath synthetic aperture radar.

Jingwen Li received the M.S. and Ph.D. degrees in electronic information engineering from Beihang University, Beijing, China, in 1988 and 1999, respectively.

Since 2000, he has been a Professor with the School of Electronic and Information Engineering, Beihang University. His current research interests include synthetic aperture radar (SAR) image processing, new SAR system design, and SAR ground moving target indication methods.

Chunsheng Li received the Ph.D. degree in signal and information processing from Beihang University, Beijing, China, in 1998.

Since 2005, he has been a Professor with the School of Electronics and Information Engineering, Beihang University. He authored more than 100 journal and conference papers and 4 books. His research interests include analysis and simulation of spaceborne synthetic aperture radar, high-resolution image formation, and multimodal remote sensing data fusion.